

## Nonlinear Dynamics of Particles Excited by an Electric Curtain

Owen D. Myers,<sup>1</sup> Junru Wu,<sup>1,2</sup> and Jeffrey S. Marshall<sup>3</sup>

<sup>1</sup>*Materials Science Program, University of Vermont, Burlington, Vermont 05405, USA.*

<sup>2</sup>*Department of Physics, University of Vermont, Burlington, Vermont 05405, USA.<sup>a)</sup>*

<sup>3</sup>*School of Engineering, University of Vermont, Burlington, Vermont 05405, USA.*

(Dated: 11 November 2014)

The use of the electric curtain (EC) has been proposed for manipulation and control of particles in various applications. The EC studied in this paper is called the 2-phase EC, which consists of a series of long parallel electrodes embedded in a thin dielectric surface. The EC is driven by an oscillating electric potential of a sinusoidal form where the phase difference of the electric potential between neighboring electrodes is 180 degrees. We investigate the one- and two-dimensional nonlinear dynamics of a particle in an EC field. The form of the dimensionless equations of motion is codimension two, where the dimensionless control parameters are the interaction amplitude ( $A$ ) and damping coefficient ( $\beta$ ). Our focus on the one-dimensional EC is primarily on a case of fixed  $\beta$  and relatively small  $A$ , which is characteristic of typical experimental conditions. We study the nonlinear behaviors of the one-dimensional EC through the analysis of bifurcations of fixed points in the Poincaré sections. We analyze these bifurcations by using Floquet theory to determine the stability of the limit cycles associated with the fixed points in the Poincaré sections. Some of the bifurcations lead to chaotic trajectories where we then determine the strength of chaos in phase space by calculating the largest Lyapunov exponent. In the study of the two-dimensional EC we independently look at bifurcation diagrams of variations in  $A$  with fixed  $\beta$  and variations in  $\beta$  with fixed  $A$ . Under certain values of  $\beta$  and  $A$ , we find that no stable trajectories above the surface exists; such chaotic trajectories are described by a chaotic (strange) attractor, for which the the largest Lyapunov exponent is found. We show the well-known stable oscillations between two electrodes come into existence for variations in  $A$  and the transitions between several distinct regimes of stable motion for variations in  $\beta$ .

---

<sup>a)</sup>Electronic mail: Junruwu@gmail.com.

## I. INTRODUCTION

The electric curtain (EC) is a device consisting of a series of parallel electrodes embedded in a dielectric surface. Alternating electric potentials are applied to these electrodes such that neighboring electrodes have a prescribed phase difference. An illustration of a two-phase EC is shown in fig. 1. Different EC geometry and control parameters, which will be defined later, make it possible to create a variety of electric fields, which can generate a wealth of physical phenomena for charged particles. For this reason, the electric curtain has been proposed for manipulation and control of particles in many different applications. Patented in 1974 by Senichi Masuda, the EC was originally invented for particle control in an electrostatic powder-painting booth<sup>1</sup>. Other proposed applications include separation of cells in the aqueous solution<sup>2</sup> and separation of by-products from agricultural processes<sup>3</sup>, transport of toner particles in photocopying machines<sup>4</sup>, mitigation of charged dust build-up for extra-terrestrial exploration of dusty planets and moons<sup>5</sup>, and separation of charged particles with different charge-to-mass ratios<sup>6</sup>.

Despite those proposed applications of ECs, few commercial applications are reported. This may be in part due to the fact that particle dynamics induced by an EC are complex and still not well understood. The motion of particles in EC fields has been studied both experimentally and computationally by a number of investigators<sup>7–14</sup>. These investigations have shown a variety of different propagating and stationary modes, including the recent report of intermittent changes of many-body particle motion discovered by Chesnutt and Marshall<sup>15</sup> in a discrete-element simulation of transport on inclined ECs.

An EC configuration whose adjacent electrodes are excited by electric potentials with less than 180 degrees of phase difference will produce a traveling-wave electric field above the surface. Particle motions in these types of fields have been found to have multifarious modes of transport, which are commonly characterized into three categories; surfing mode, hopping mode, and curtain mode<sup>12</sup>. In the surfing mode, particles travel synchronously with the wave front, whereas in the hopping mode particles will stick to the surface and hop stochastically when freed by a sufficiently strong electrostatic force or collision with another particle. In the curtain mode, high frequency electric field oscillations force particles to be levitated above the electrode surface and travel in a spiraling trajectory with considerably slower average forward progression speed than the propagation velocity of the traveling wave.

In this paper we discuss the particle nonlinear motion in an electric field generated by a two-phase EC, which has been called a standing wave<sup>1,5</sup> EC. For some time it was believed that this type of EC would have poor transport properties<sup>1,5</sup>. However, recently both experiments<sup>16,17</sup> and numerical computations<sup>9</sup> have demonstrated that 2-phase ECs can be very effective at transporting particles, and in fact particles will exhibit two very distinct modes of transport under different conditions. The relative simplicity of the 2-phase EC makes it an attractive candidate for many of the proposed applications.

A significant amount of work has been reported on ECs, but the nonlinear dynamics of the particles within an EC field have not been studied in detail from a dynamical systems point of view. Using simple mathematical models we have discovered very prolific behaviors of charged particles in a two-phase oscillating EC electric field. A detailed understanding of the rudimentary particle motions might help us better interpret the complex phenomenon often observed in real EC experiments.

To simplify the mathematical presentation, we have only considered  $1D$  and  $2D$  motion of a single charged particle. While this is a very simple system, it is nevertheless sufficient to exhibit a rich variety of dynamical behavior. Using a similar method to that outlined by Masuda and Kamimura<sup>18</sup> for 3-phase ECs, an approximate analytical equation has been derived for the motion of a charged particle in the 2-phase EC electric field. In general, motion of a single charged particle in the field of the 2-phase EC is two-dimensional, provided that no initial motion in the direction along the electrodes is introduced. However, a special case of one-dimensional particle motion, in which the electric field magnitude is insufficient to lift a particle initially located on the dielectric surface of the EC, is found to generate highly interesting particle behavior.

It is worthwhile to point out that the equations of motion contain a time-dependent potential, similar to the parametrically driven pendulum with a vertically oscillating suspension point, which is known to have interesting dynamical properties<sup>19–21</sup>. Our derived equations of motion are solved numerically and the behaviors of the particle motions induced by the oscillating electric field are examined. We obtain limit cycles which are fixed points in the appropriate Poincaré sections of the phase space, and bifurcations of these fixed points that lead to chaotic motions for a range of interaction amplitude values (a dimensionless parameter containing the amplitude of electrode linear charge density and the charge carried by a particle). Linear stability for very small interaction amplitude can be analyzed using a

special case of the Mathieu equation<sup>22–25</sup>. As we increase the interaction amplitude, we show a variety of interesting trajectory types in the 1D limit and several predominant trajectories for the 2D cases.

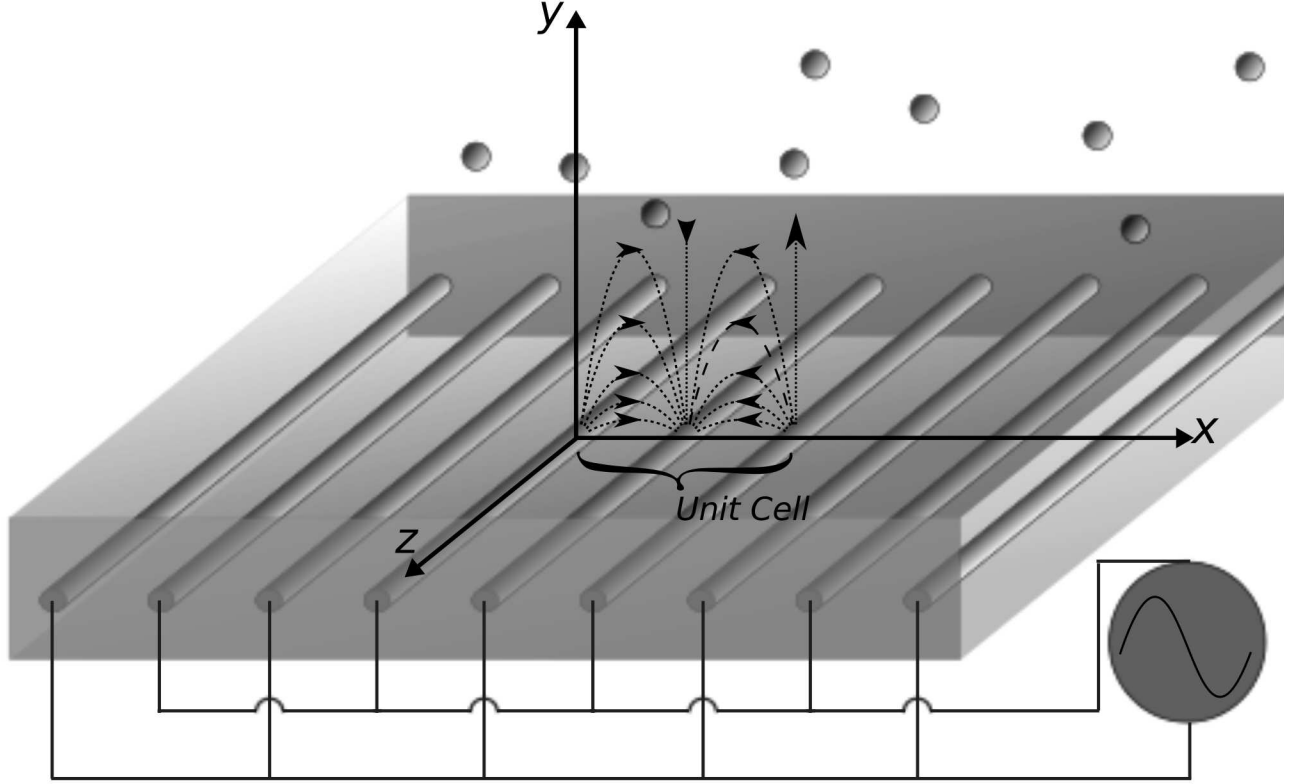


FIG. 1. Transparent view of a 2-phase EC with our choice of axes are super imposed. The dashed lines represent the electric field lines in the positive  $y$  plane. The 2-phase EC is periodic over the set of electrodes marked as the "unit cell".

## II. METHODS

### A. Model Equations

Our model uses the so-called centerline charge approximation, in which a set of parallel electrodes in the  $x, z$  plane of the Cartesian coordinates are considered to be line filaments of infinite length oriented along the  $z$ -direction<sup>18</sup>. The  $x$ - $y$  plane is chosen to be orthogonal to the electrode axes ( $z$ -axis) as shown in fig. 1, where the  $x$  and  $y$ -axes are parallel and

perpendicular to the dielectric surface, respectively. To find the electric potential and electric field above the plane of the electrodes produced by the set of equally spaced 2-phase electrodes, we adopt the conformal transformation used by Masuda and Kamimura<sup>18</sup>:

$$e^{(-y+ix)2\pi/\lambda} = u + iv. \quad (1)$$

This transformation maps the  $x, y$  ( $y > 0$ ) half-plane containing infinite numbers of periodic electrodes into a unit circle in the  $u, v$  complex plane containing just two electrodes. Therefore, the electric potential can be easily computed in the  $u, v$  plane. The inverse conformal transform is then performed to map the expression back to  $x - y$  coordinates. The detailed derivation is given in Appendix A. Based on the derivation, the electric potential can be simply expressed as:

$$\Phi(x, y) = \frac{-Q}{4\pi\epsilon_0} \cos \omega t \ln \frac{\cosh ky + \cos kx}{\cosh ky - \cos kx}$$

.

Using  $\mathbf{E} = -\nabla\Phi$  the electric field in the  $x$  and  $y$  directions is found to be

$$E'_x = \frac{kQ}{2\pi\epsilon_0} \sin(kx') \cos(\omega t') \frac{\cosh(ky')}{\cosh^2(ky') - \cos^2(kx')}, \quad (2)$$

$$E'_y = \frac{kQ}{2\pi\epsilon_0} \sinh(ky') \cos(\omega t') \frac{\cos(kx')}{\cosh^2(ky') - \cos^2(kx')}, \quad (3)$$

where  $Q$  is the linear charge density amplitude of an electrode,  $m$  and  $q$  are the mass and electric charge carried by a particle, respectively,  $k$  is the wave number, and  $\omega$  is the angular driving frequency of the driving electric fields. It is noted that we use the primed variables here to save unprimed variables for their dimensionless counterparts, which are defined below. For the centerline charge approximation to be valid it is required that the dielectric surface be located a minimal distance above the electrodes<sup>18</sup>. However, if the surface is far from the electrodes, the cosh-term on the right-hand side of Eq. (2) and Eq. (3) diminishes as  $1/\cosh y' \sim e^{-y'}$  and consequently the electric field magnitude rapidly approaches zero.

The dimensionless time, horizontal and vertical positions are defined by  $t = \omega t'$ ,  $x = kx'$ , and  $y = ky'$ . A dimensionless interaction amplitude ( $A$ ), gravitational acceleration ( $g$ ) and damping coefficient ( $\beta$ ) are, respectively, defined by  $A = \frac{k^2 q Q}{4\pi\epsilon_0 m \omega^2}$ ,  $g = g'k/\omega^2$ , and

$\beta = \beta'/m\omega$ , where  $\beta'$  is the damping coefficient, and  $g'$  is the gravitational acceleration. The dimensionless form of the differential equations governing the particle motion are:

$$\frac{d^2x}{dt^2} + \beta \frac{dx}{dt} = A \sin x \cos t \frac{2 \cosh y}{\cosh^2 y - \cos^2 x}, \quad (4)$$

$$\frac{d^2y}{dt^2} + \beta \frac{dy}{dt} = A \sinh y \cos t \frac{2 \cos x}{\cosh^2 y - \cos^2 x} - g. \quad (5)$$

Letting the dimensionless spacing of the distance between neighboring electrodes be  $\pi$ , the system is periodic over a distance  $\lambda = 2\pi$  in  $x$ . We choose the dielectric surface to be at  $y = 1$ , i.e.  $y' = 1/k = \lambda/2\pi$ , for which the centerline charge approximation holds.

## B. Distinction of One and Two Dimensional Regimes

Two distinct regimes are considered: (1) A one-dimensional regime where the particle is constrained to roll or slide back and forth on the dielectric surface; (2) a two-dimensional regime where the particle moves in the x-y plane, either being levitated above the surface or bouncing off of it. Dissipative forces are included in the model for both regimes. For the  $1D$  regime, dissipative forces may arise both from rolling resistance between the particle and the surface and from the viscous fluid force (Stokes drag) between the particle and the surrounding air. Both of these dissipative forces are proportional to the particle velocity<sup>26</sup>. In the  $2D$  case, the particle is assumed to have elastic collisions with the dielectric surface, so the only dissipation is from fluid drag force. The transition from motion on the surface ( $1D$ ) to the  $2D$  regime occurs when the maximum vertical force imposed on a particle immediately above an electrode exceeds the gravitational force on the particle. For a charged particle attached to the dielectric surface, the electric field is evaluated at a value of  $y$  equal to the particle centroid position. Letting the gravitational force balance the maximum electrostatic force, the maximum value of the interaction amplitude  $A$  for which the particle remains on the surface can be obtained by setting the left-hand side of Eq. (5) to zero, giving

$$\frac{A}{g} \leq \frac{\cosh^2 y - 1}{2 \sinh y} \quad (6)$$

With the location of the surface at  $y = 1$ , the critical value of this ratio for which the  $1D$  approximation applies is obtained as  $A/g \leq 0.588$ . In order to further simplify this system,

we neglect the adhesive van der Waals force. This simple system is used to examine the nonlinear dynamics for small variations over a range of  $A$  with constant values of  $\beta$ .

### III. TIME MAPS

We classify different trajectories by the periodicity of their limit cycles in the full phase space. The interaction amplitude, damping, and initial conditions determine the periodicity of the particle trajectory. We compare the temporal length of a limit cycle to the inverse of the driving frequency of the electric field by using time maps. Time maps are used to represent the advancement of an orbit in phase space by some amount of time. In general, a particle's position and velocity determine its position in phase space, which can be represented as a vector function  $\mathbf{r}(\mathbf{r}_0, t)$ , where  $\mathbf{r}_0$  is the initial position in the phase space. We choose the time maps to be represented in the form  $\mathbf{f}(\mathbf{r}_0, t = 2\pi n)$ . The time mapping gives a stroboscopic view of the parametric function  $\mathbf{r}$  when  $n$  is a positive integer ( $\mathbb{Z}^+$ ). For  $n \in \mathbb{Z}^+$  the time mapping highlights the relationship between the period of a trajectory and the driving frequency. We define an operator  $\mathbf{T}$  that maps the system forward in time by  $2\pi$ , so that the function  $\mathbf{f}(\mathbf{r}_0, t = 2\pi n)$  may be written as  $\mathbf{T}^n \mathbf{r}$ .

The 2D EC has five degrees of freedom  $x, y, \dot{x}, \dot{y}, t$ . The periodicity of the system in  $x$  and  $t$  implores the use of a toroidal phase space. We use this notion of a toroidal phase space to fashion our Poincaré sections. We defer to the 1D EC in order to visualize the toroidal phase space (fig. 2). For the 2D EC we cannot graphically depict the full phase space but we use the same periodic geometries to fashion Poincaré sections. A Poincaré section includes any point where a continuous trajectory or flow transversely intersects a subspace of the space the trajectory occupies<sup>27</sup>. Strobing a periodically driven system will produce Poincaré sections of  $d - 1$  dimension, where  $d$  is the dimension of the full phase space. This is equivalent to observing time maps  $\mathbf{T}^n$  acting on a point in phase space. It becomes apparent that this method of strobing or time mapping produces Poincaré sections when we look at a particle's trajectory as a function of time  $t$  passing through a  $x, \dot{x}$  phase plane at a particular time  $t$ . The particles path is always transverse to the  $x, \dot{x}$  plane and therefore a point of intersection of the trajectory with this plane is a convenient sub space that satisfies the criterion necessary to be a Poincaré section. It is also true that time maps generate Poincaré sections for the 2D EC, but in this case the mappings represent intersections of



a trajectory with a non-planar subspace. This is still a Poincaré section because the flow through the subspace is guaranteed to be transverse to it due to the positive rate of change of time.

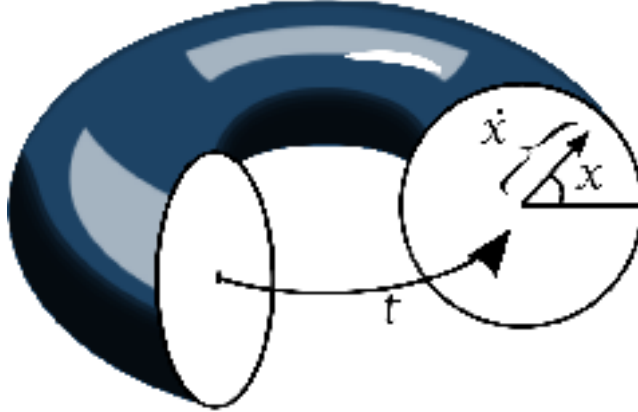


FIG. 2. Due to the periodicity of the EC in the  $x$ -direction, and the periodic fluctuations of the electric field with time, it is useful to use toroidal geometry to describe the 1D EC phase space. We define the  $t$ -axis as the line at the major radius when the minor radius is zero. The position and velocity at a given time may then be represented as a point in the plane orthogonal to the time axis described by an angle ( $x$ ) and radius ( $\dot{x}$ ). The origin of this plane is located at the intersection with the  $t$ -axis.

By filling a plane in phase space with an array of initial conditions, a large number of possible trajectories can be obtained for given values of  $\beta$  and  $A$ . For instance, in 1D simulations initial conditions are prescribed in the  $x - \dot{x}$  plane at  $t = 0$ . For 2D simulations, initial conditions are prescribed on a planar section of the four-dimensional phase space at  $t = 0$ . Different initial planes are used to explore different regions of the phase space. We define a region of phase space filled with an array of initial conditions as a *block*. A group of positions in the phase space at a given time is represented by a  $2 \times N$  dimensional matrix  $\mathbf{B}$ , where the first index (2) is the dimensionality of the block and the second index ( $N$ ) is the number of different initial conditions in the block. The advancement of these initial conditions in phase space by intervals of the driving period can be represented with time maps by  $\mathbf{T}^n \mathbf{B}$ . The different attractors in the system can be found by taking  $\mathbf{T}^n \mathbf{B}$  as  $n \rightarrow \infty$ . As discussed above, a series of time maps can be used to generate a Poincaré sections of  $\mathbf{B}$  in the phase space.

## IV. RESULTS

### A. One Dimensional Regime

For small  $A$  and finite  $\beta$ , a particle on the dielectric surface will drift toward the nearest electrodes. For an electrode located at  $x = 0$ , an analytical solution can be obtained for particles at small distances  $|x|$  from the electrode. Using the leading-order Taylor series approximations  $\sin x \approx x$  and  $\cos x \approx 1$ , the multiplying factor in Eq. (4) can be approximated as

$$\frac{2 \cosh y}{\cosh^2 y - \cos^2 x} \approx \frac{2 \cosh y}{\cosh^2 y - 1} \equiv C, \quad (7)$$

where  $C$  is a constant for  $y = 1$ . The equations of motion then become

$$\frac{d^2 x}{dt^2} = ACx \cos t - \beta \frac{dx}{dt}. \quad (8)$$

Under the transformation  $x(t) = e^{(-\beta t/2)} u(t)$  and  $t = 2\theta$  it takes the form<sup>25</sup>

$$\frac{d^2 u}{d\theta^2} = u(a - 2q \cos 2\theta), \quad (9)$$

where  $q = AC/8$  and  $a = -\beta^2$ . Equation (9) is the canonical form of the Mathieu equation. There are infinite sets of alternating stable (periodic) and unstable solutions for variation of the parameters  $a$ ,  $q$ <sup>28</sup>. Here we are only interested in the bound solutions because unstable trajectories force the consideration of larger  $|x|$  for which this approximation breaks down. The function  $u(t)$  may be expressed as a linear combination of the cosine and sine type elliptic functions. It is well known that the stability of the elliptic functions depends on the parameters  $a$  and  $q$ . The stability boundary may be expressed as a function  $q(a)$ . Gunderson et al.<sup>29</sup> derive a condition for asymptotic stability based the relationship between the two parameters. The inequality found by Gunderson et al. that needs to be satisfied for asymptotic stability in the EC takes the form  $A < \beta^2/2C$ . This relationship only holds for small  $a$  and  $q$ , but so does the analytical treatment of the EC. We refer the reader to McLachlan<sup>25</sup> for a thorough description of elliptic functions and their different representations.

For larger values of  $A$ , particles are not necessarily confined above the electrodes. In order to analyze this system and highlight the dimensionality of the full phase space, it

is convenient to express Eq. (4), with  $y = 1$  denoting the dielectric surface, as a set of first-order autonomous differential equations.

$$\begin{aligned}\dot{x}_1 &= x_2 \\ \dot{x}_2 &= A \sin x_1 \cos x_3 \frac{2 \cosh 1}{\cosh^2 1 - \cos^2 x_1} - \beta x_2 \\ \dot{x}_3 &= 1\end{aligned}\tag{10}$$

The following transformations used in Eq. 4 give us Eq. 10:  $x \rightarrow x_1$ ,  $\dot{x} \rightarrow x_2$ , and  $t \rightarrow x_3$ . We know from the previous discussion of time maps that a period- $p$  fixed point in the Poincaré sections, located at  $\mathbf{r}_{fp}$  in the phase plane  $x_1$   $x_2$  is defined by  $\mathbf{T}^{pn}\mathbf{r}_{fp} = \mathbf{r}_{fp}$ , where  $n \in \mathbb{Z}^+$ . A period- $p$  orbit (i.e limit cycle) is one which repeats itself after  $p$  driving cycles. All Poincaré sections obtained by sequential time maps have two fixed points within the toroidal phase space (see fig. 2) located at  $x_1 = 0$  and  $x_1 = \pi$ . These fixed points are representative of limit cycles of period-1 in the phase space. These two limit cycles are the only invariant sets in the full parameter and phase space which exist for all values of  $A$  and  $\beta$ . For definiteness, we define  $\mathbf{r}_{fp1}$  to be the  $x_1 = \pi$ ,  $x_2 = 0$  fixed point in the Poincar sections. To distinguish between the fixed point in the Poincaré section and the corresponding limit cycle in the phase space, we define the full invariant set composing the limit cycle as  $\{\mathbf{r}_{fp1}\}$ , where the curly brackets denote a set.

In general, the stability of a fixed point in the Poincaré section can be analyzed using Floquet theory<sup>30</sup>, details of which are provided in Appendix B. By integrating the linearized equations of motion about a periodic orbit with periodicity  $p$ , a solution for small perturbations of the fixed-point solution lying on the closed orbit is obtained. A similar approach is illustrated in<sup>19</sup> for Floquet theory applied to the parametrically driven pendulum which is mathematically similar to the 1D EC. The eigenvalues (Floquet stability multipliers)  $\lambda_1$ ,  $\lambda_2$  are generally complex, where a fixed point in the Poincaré section is unstable when the magnitude of  $\lambda_1$  or  $\lambda_2$  is greater than unity. In cases where there is no analytical expression for a fixed point as a function of  $A$ , a polynomial curve fit is used to estimate the fixed point as a function of  $A$ .

We initially focus attention on the  $\beta = 0.1$  case because this value is typical of a variety of realistic EC configurations. A bifurcation diagram for this case is shown in fig. 3. The points corresponding to each value of  $A$  in this bifurcation diagram are obtained by plotting

the positions of a block of 1830 different initial conditions covering the region  $0 \leq x_1 < 2\pi$  and  $-1.5 \leq x_2 \leq 1.5$ , plotted after 637 time maps. This process is repeated for different  $A$  values ranging from 0 to 0.4, in steps of 0.0008. In order to indicate the number of initial conditions corresponding to each point in this diagram, a hexagonal histogram was formed in which the  $x_1$ -position is discretized into 400 bins. The color bar in fig. 3 represents the logarithm of the number of points in the corresponding bin.

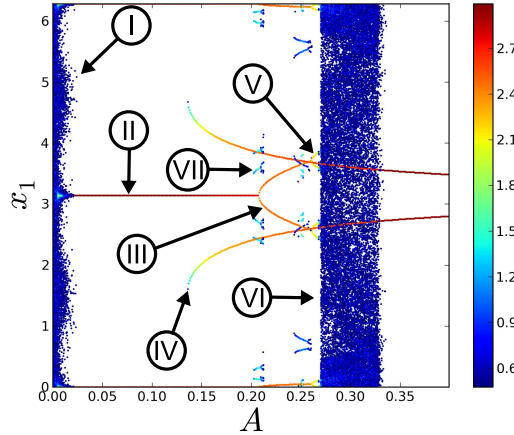


FIG. 3. A bifurcation diagram made by taking a two dimensional histogram of the final Poincaré section of 1830 different initial conditions for 500 different values of  $A$ .  $\beta$  is set to 0.1. Roman numerals denote the individual features focused on in the paper; Region I: With  $A$  being close to zero transients take a long time to die out. Region II: A stable fixed point above the electrode representing a sink where particles are stationary. Region III: A period-2 orbit oscillating about the electrode. Region IV: Stable propagating trajectories with comparatively high speeds. Region V: Four fixed points in the digram representing two period-2 trajectories born out of a cyclic fold bifurcation. Region VI: Period doubling leads to chaotic motion. Region VII: A period-4 fixed point in the Poincaré sections that discontinuously appears and disappears over variations of  $A$ .

For very small values of  $A$ , denoted by region I in fig. 3, the  $x_1$  position of the points in this figure are widely dispersed. This scattering occurs because the transients are very slow to die out for small values of  $A$ , and therefore the block of initial conditions has not yet reached its final state. As we increase  $A$ , a single line is observed in the fig. 3, denoted by region II, representing the  $\mathbf{r}_{fp1}$  attractor. For these values of  $A$ , this attractor is an asymptotically stable fixed point in the Poincaré sections, so that initial conditions in a

small neighborhood about  $\mathbf{r}_{fp1}$  map to  $\mathbf{r}_{fp1}$ . In regimes I and II, the direction of the time-averaged force on the particle points to locations of constant electrostatic potential. This condition is similar to the well-known Bjerknes force in acoustics<sup>31</sup>, wherein the acoustic radiation force on a particle points to either the nodes or antinodes of a standing acoustic field. The fixed point  $\mathbf{r}_{fp1}$  remains asymptotically stable for values of  $A$  in the interval  $0 < A < A_{c1}$ , where  $A_{c1} \equiv 0.20761 \pm .00001$ .

At  $A = A_{c1}$ , a bifurcation of the  $\mathbf{r}_{fp1}$  fixed point is observed, beyond which the single line splits into two period-2 curves, which are symmetric about the  $x_1 = \pi$  line as indicated in region III in fig. 3. The real and imaginary parts of the two Floquet stability multipliers,  $\lambda_1$  and  $\lambda_2$ , for  $\mathbf{r}_{fp1}$  including values of  $A$  close to  $A_{c1}$  are shown in fig. 4. The discontinuity in fig. 4, where the imaginary parts go to zero, represents the transition of the fixed point from an attracting focus to an attracting node. The point at which  $\lambda_2$  decreases below  $-1$  in fig. 4 corresponds to the bifurcation, where  $\mathbf{r}_{fp1}$  becomes a period-1 saddle. Beyond this bifurcation, the fixed point becomes linearly unstable in what is called a supercritical flip bifurcation. The instability of the period-1 saddle creates a stable limit cycle of period-2 about  $\mathbf{r}_{fp1}$ . It may be surprising that the first oscillations are not period-1. This is because period-1 oscillations are not a harmonic of  $\mathbf{r}(t)$ <sup>20</sup>. There are, however, two period-1 fixed points apparent in fig. 3 seen for  $A > 0.13$  (one on either side of  $x = \pi$ ) denoted by region IV which represent propagating trajectories. These propagating trajectories travel once through the toroidal phase space per driving cycle making them period-1 fixed points in fig. 3 but they are not periodic oscillations because they are constantly traveling in one direction.

We call the uppermost region III curve  $\mathbf{r}_{fp2}$ .  $\mathbf{r}_{fp2}$  is an attracting focus for values of  $A \leq 0.234$ . Just as in the first bifurcation, the attractor  $\mathbf{r}_{fp2}$  transitions to an attracting node shortly preceding the second bifurcation, which occurs at  $A = A_{c2}$ , where  $A_{c2} \equiv 0.26077 \pm 0.00001$ . A close-up view showing this bifurcation is given in fig. 3b. This bifurcation is of the type known as a cyclic fold bifurcation, where the fixed point becomes unstable and the symmetry of the trajectory corresponding to the fixed point is broken at the bifurcation point. As  $A$  is increased through  $A_{c2}$  two new possible trajectories are spontaneously created denoted by region V in fig. 3. The initial conditions determine which of the new possible trajectories a particle will settle into. As the particle trajectory is known to be highly sensitive to small changes in initial condition, this type of bifurcation is

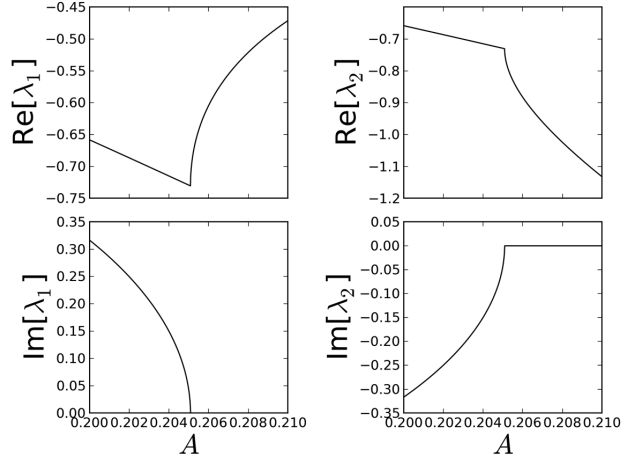


FIG. 4. Floquet stability multipliers of the  $(x = \pi, \dot{x} = 0)$  fixed point for a range of  $A$  in which the first bifurcation occurs. The discontinuity is the transition from an attracting focus to an attracting node. The supercritical flip bifurcation happens as  $\text{Re}[\lambda_2]$  becomes smaller than  $-1$ .

known to produce hysteresis for processes in which  $A$  is varied about  $A_{c2}$ <sup>32</sup>. An alternative viewpoint of this bifurcation sequence is given by plotting projections along the  $x_3(t)$  axis of the phase space onto the  $x_1, x_2$  plane for some particular values of  $A$  in fig. 5a. This figure shows the fixed point  $\mathbf{r}_{fp1}$  bifurcating into a sequence of limit cycles, denoted in the Poincaré section by  $\mathbf{r}_{fp2}(A)$ , as  $A$  is increased past  $A = A_{c1}$ . These curves are point symmetric about  $(x_1 = \pi, x_2 = 0)$  in the interval  $A_{c1} < A < A_{c2}$ . For  $A > A_{c2}$ , two families of trajectories are observed, one of which shifts in the positive  $x$ -direction and the other shifts in the negative  $x$ -direction, breaking the point symmetry. We only show one of the two possible trajectories for  $A > A_{c2}$  in figure 5a for clarity. Sample trajectories for each of these intervals are plotted on the  $x_1, x_2$  plane in fig. 5b to highlight the symmetry breaking. The first bifurcation at  $A = A_{c0}$  looks geometrically similar to a Hopf-bifurcation in fig. 5a, but this is an artifact of the projection process along  $x_3$ , where in fact the  $\{\mathbf{r}_{fp1}\}$  set that gives rise to the  $\mathbf{r}_{fp1}$  fixed point in fig. 5a is a limit cycle rather than an equilibrium point in time.

Following this second bifurcation (region V), a series of period-doubling bifurcations occurs, with the first of these bifurcations happening at  $A = A_{c3}$ , where  $A_{c3} \equiv 0.26798 \pm 0.00001$ . Table I shows the values of  $A$  at which each period-doubling bifurcation occurs, the period of the limit cycle after the bifurcation and the type of bifurcation. It can be seen in fig. 3 that the period doubling cascade initial occurs in a very small range of  $x$ ; in fact, it occurs

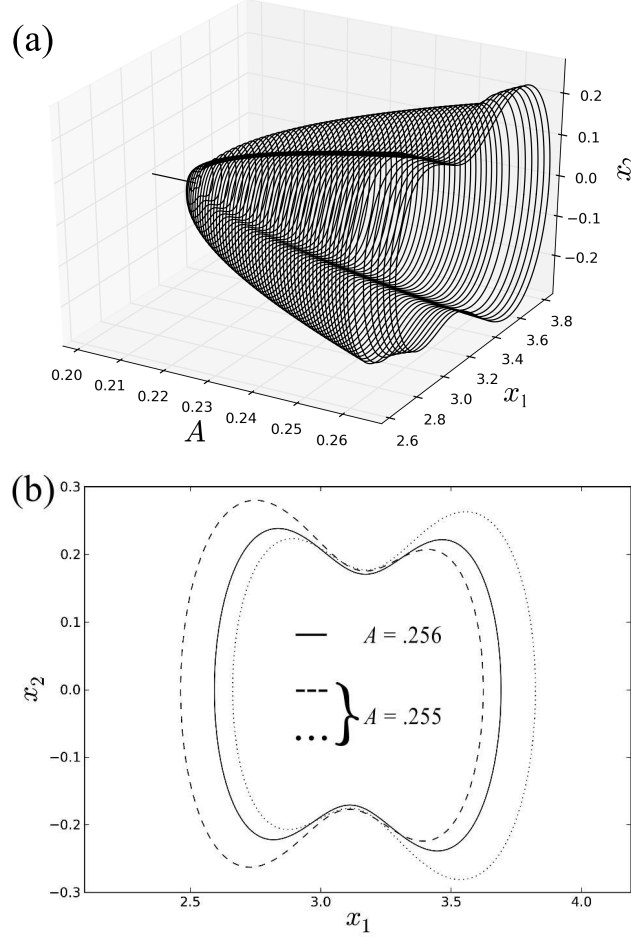


FIG. 5. (a) projections of the full phase space onto the  $x_1$ ,  $x_2$  axes for a range of  $A$  that includes the first two bifurcations. The first being a supercritical flip bifurcation and the second being a cyclic fold bifurcation. (b) Solid line: Trajectory after supercritical flip but before cyclic fold. Dashed and dotted lines: The two possible trajectories after cyclic fold.

in a very small volume of the full phase space. The density of the higher period trajectories, even after the period-32 bifurcation, make it extremely difficult to distinguish periodicities. Using  $A_{c3}$ ,  $A_{c4}$ , and  $A_{c5}$  we calculate the Feigenbaum constant  $\delta$  to be 4.2000. Using  $A_{c4}$ ,  $A_{c5}$ , and  $A_{c6}$  we calculate the Feigenbaum constant to be 4.4643. This progression looks as though it might lead to the universal value of  $\delta \approx 4.6692^{33}$ . The Feigenbaum constant  $\delta$  can be evaluated with

$$\delta = \lim_{n \rightarrow \infty} \frac{A_{cn-1} - A_{cn-2}}{A_{cn} - A_{cn-1}}. \quad (11)$$

TABLE I. Period Doubling Bifurcations

$A_{cn}$	Bifurcation	$A$	Period of New Limit Cycle
$A_{c1}$	Supercritical Flip	$0.20761 \pm 0.00001$	2
$A_{c2}$	Cyclic Fold	$0.26077 \pm 0.00001$	2
$A_{c3}$	Supercritical Flip	$0.26798 \pm 0.00001$	4
$A_{c4}$	Supercritical Flip	$0.26903 \pm 0.00001$	8
$A_{c5}$	Supercritical Flip	$0.26928 \pm 0.00001$	16
$A_{c6}$	Supercritical Flip	$0.269336 \pm 0.000002$	32

$A_{cn}$  are the values of  $A$  for which a period-doubling bifurcation occurs,  $A_{cn}$  being the  $n^{th}$  bifurcation. As  $A$  is increased, the period-doubling cascade leads to a chaotic regime, identified by the scattered points denoted by region VI in fig. 3. This chaotic state exhibits a strange attractor, which consists of a region in phase space with fractal geometry to which particle trajectories approach as  $t \rightarrow \infty$ . A Poincaré section of the strange attractor for this system is plotted in fig. 6. As shown in fig. 7f, this chaotic state exists simultaneously with the two stable period-1 limit cycles (region IV), where the latter have substantial higher velocity magnitude than the points in the chaotic state. The basins of attraction for the strange attractor and the stable limit cycles are plotted in fig. 7 for  $A = 0.3$ , along with plots showing the evolution of these basins in time as they approach their respective attractors. We have found the largest Lyapunov exponent for this chaotic attractor to be  $0.165 \pm 0.001$ . In general The largest positive Lyapunov exponent is a way of quantifying the strength of chaos. More specifically it is the measure of the rate with which two infinitesimally close initial conditions in phase space will separate. We have calculated the largest Lyapunov exponent by comparing a fiducial trajectory to a neighbor placed infinitesimally close. After a small period of time we re-orient the perturbed trajectory along the vector for which there was maximal separation. By continuing this process for many iterations and throwing away the transients we find the maximum separation of the perturbed trajectory from the fiducial trajectory. With these data it is straight forward to calculate the Lyapunov exponent<sup>32</sup>.

The last feature we focus on in fig. 3 are the stable limit cycles that appear and disappear discontinuously for small variations in  $A$ . We have chosen one of these limit cycles (denote as region VII in fig. 3a) to analysis the stability in order determine the nature of its



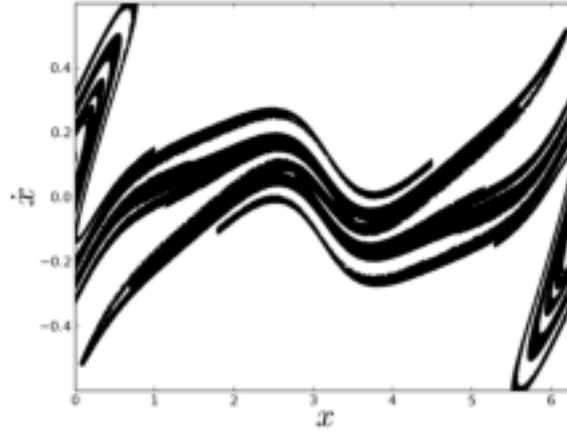


FIG. 6. A Poincaré section of the strange attractor found when  $A = 1.3$ . The figure was made by letting a trajectory approach the attractor for a long time and then plotting successive Poincaré sections when it was assumed to be close if not in the attractor

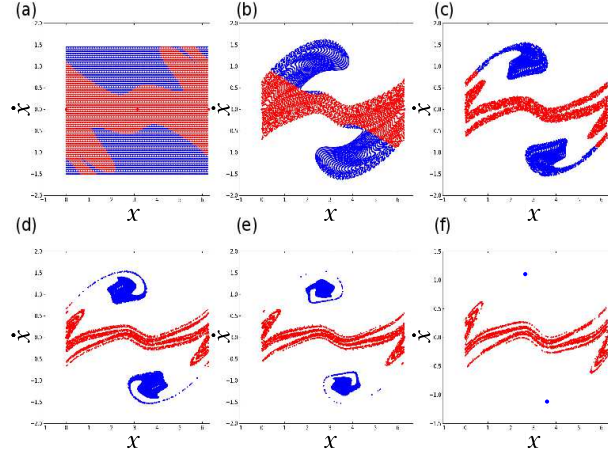


FIG. 7. (a) Block  $B$  of initial conditions colored red if they are in the basin of attraction of the strange attractor and blue if they are in the basin of the coexisting fixed points. (b)  $B$  after time map  $T^1$ . (c)  $T^2 B$ . (d)  $T^3 B$ . (e)  $T^4 B$ . (f)  $T^{300} B$ .

creation and disappearance. In fig. 3 four fixed points appear as  $A$  is increased through  $0.20182 \pm 0.00001$ . These fixed points correspond to a period-4 limit cycle shown in fig. 8 for  $A = 0.2086$  projected on the  $x_1, x_2$  plane. This limit cycle is point-symmetric about  $(x_1 = \pi, x_2 = 0)$  but as  $A$  is increased further the limit cycle breaks its point symmetry in a cyclic fold bifurcation before undergoing a period doubling cascade.

A comparative study was performed for this system for different values of the damping

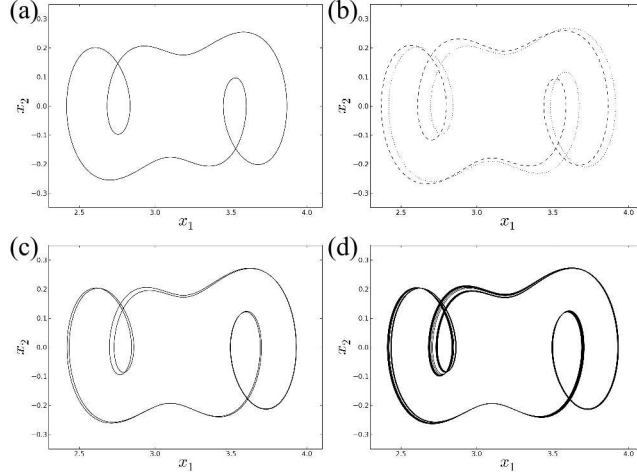


FIG. 8. (a) A period-4 trajectory that creates the initial region VII (3) fixed points. (b) The two possible period-4 trajectories after a cyclic fold bifurcation distinguished by the dashed and dotted lines. (c) After the dotted line in (b) undergoes a supercritical flip and its period doubles. (d) The result of more period doubling bifurcations.

coefficient  $\beta$ . Bifurcation plots showing particle positions in the Poincaré sections versus the interaction amplitude  $A$  are given in fig. 9 for  $\beta = 0.01, 0.05$ , and  $0.2$ , which are indicative of systems with very little damping, moderate damping and heavy damping, respectively. All of these plots exhibit the region IV stable propagating period-1 limit cycles and initial stability of the  $\mathbf{r}_{fp1}$  fixed point at  $x_1 = \pi$ . In the cases of  $\beta = 0.05$  and  $0.2$ , the  $\mathbf{r}_{fp1}$  attractor exhibits a period-doubling bifurcation, similar to that discussed above for the  $\beta = 0.1$  case, followed by a sequence of bifurcations to a chaotic state. The  $\beta = 0.01$  case, by contrast, does not appear to have a clear bifurcation of the  $\mathbf{r}_{fp1}$  attractor. The next most evident difference between the bifurcation diagrams is the number of trajectories that discontinuously appear and disappear as  $A$  is increased. For  $\beta = 0.2$  we see fewer of these disconnected fixed points, one set being very similar to the fixed points associated with the limit cycles shown in fig. 8. Clearly the bifurcation sequence to the chaotic attractor, the chaotic state itself, and the higher velocity propagating trajectories are the dominate features in the larger  $\beta$  phase space.

We briefly continue our investigation past the first chaotic regime. We find that as we continue to increase  $A$  there are alternating arrangements of chaotic and non-chaotic solutions. In fig. 10a we show the next stable regime and its transition to chaos in a

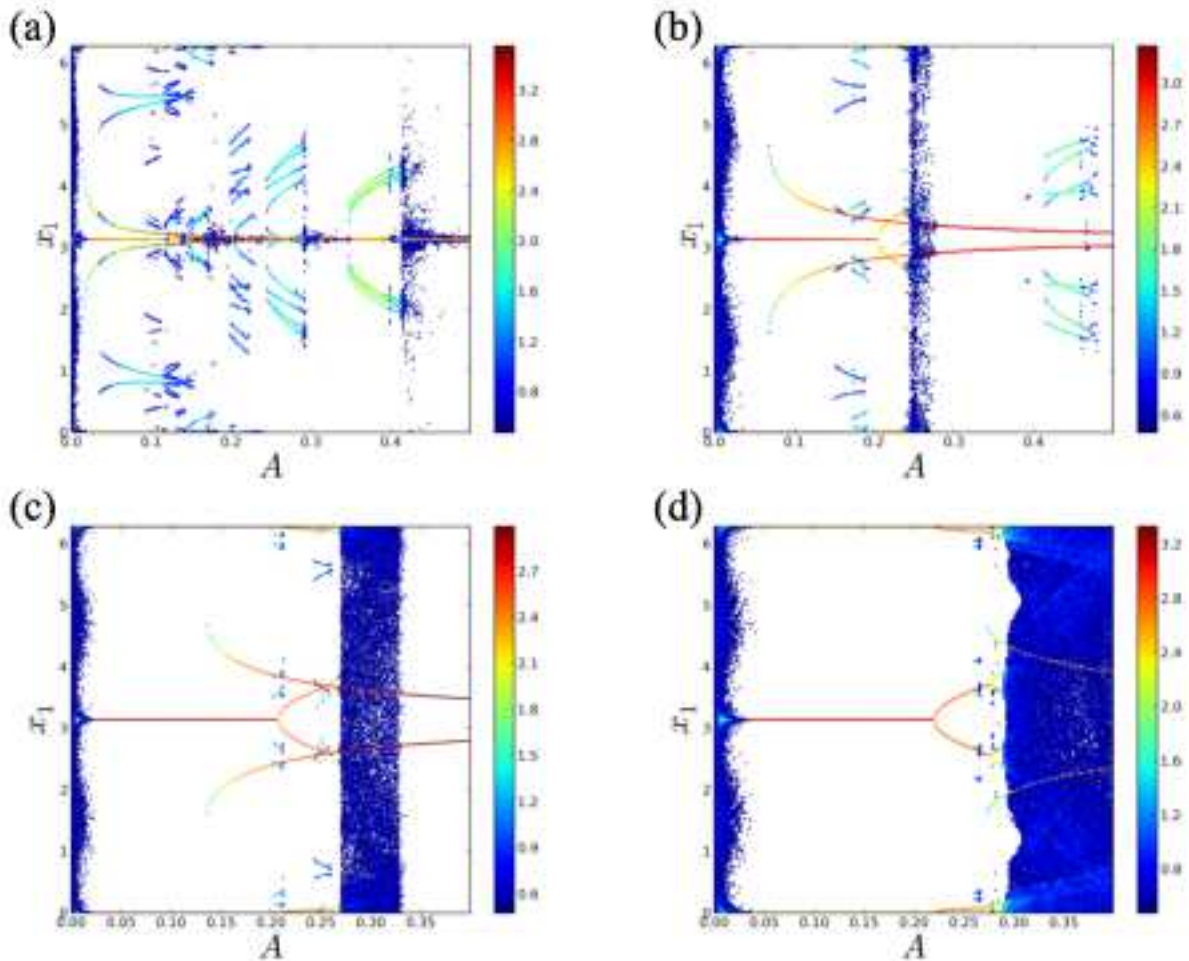


FIG. 9. Bifurcation diagrams computed using the same methods as in fig. 3. (a)  $\beta = 0.01$ . (b)  $\beta = 0.05$ . (c)  $\beta = 0.1$ . (d)  $\beta = 0.2$ .

bifurcation diagram. In fig. 10b we show the chaotic attractor for  $A = 1.7$  and the largest Lyapunov exponent for this value of the interaction amplitude is found to be  $0.187 \pm .003$ .

## V. TWO DIMENSIONAL REGIME

In the 2D EC the additional force of gravity in the equations of motion make the system codimension 3. For the rest of this discussion we set  $g = 0.1$  because for certain values of  $A$  and  $\beta$  it is found to produce results on a convenient dimensionless timescale that are similar to those discussed in the literature<sup>5,13,16,17,34–36</sup>. It is worth clarifying this choice of  $g$  because it may seem that  $g = 0.1$  and our choice of  $A$  values in the 1D EC section violate the inequality in Eq. (6). This issue is rectified by choosing the appropriate  $k$  and  $\omega$  for the

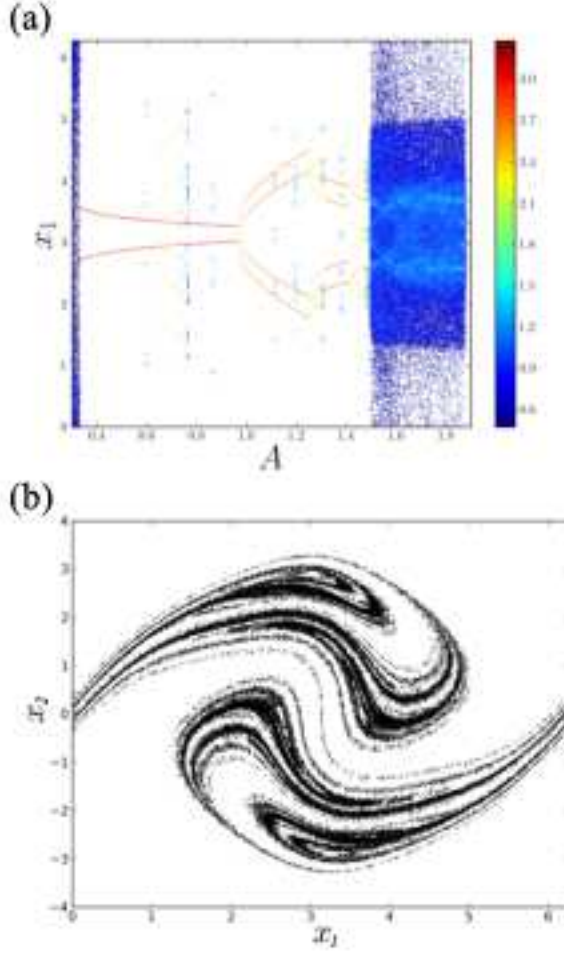


FIG. 10. (a) bifurcation diagram for the second range of stable motion as well as a transition to a second chaotic regime. (b) The chaotic attractor found for  $A = 1.7$ .

1D EC where the ratio  $k/\omega$  is quadratic in  $A$  and linear in  $g$  making it possible to balance  $A/g$  so that Eq. (6) is satisfied. We focus primarily on particle motion in the  $x, y$  plane for ease of comparison to previous and future experimental work

To begin the study of the two dimensional regime we fix the damping at  $\beta = 0.1$  and then sweep through the interaction amplitude from  $A = 0.1$  to  $A = 25$ . We use the same methods in making the bifurcation diagrams as those used in making the 1D EC bifurcation diagrams. Even when no bifurcating fixed points are found this methodology is an informative way to explore the 2D EC dynamics. In fig. 11a the final Poincaré sections used to make the diagram were projected onto the  $x$  axis and in fig. 11b the Poincaré sections were projected onto the  $y$  axis. In fig. 11a there are two red lines trisecting the diagram in the horizontal direction as well as a background of scattered points. The two red lines are asymptotically

stable fixed points (attractors) in the Poincaré sections that exist for all  $A$  above  $A \approx 0.3$ . These fixed points in the Poincaré sections are located directly in-between the electrodes. In fig. 11b there is only one red line with the background of scattered points implying both fixed points are located at the same  $y$  for a given  $A$ . In fig. 11a it is also clear that the location of these fixed points increases in  $y$  as  $A$  is increased. The two fixed points are period-2 limit cycles. They do not contact the surface and they oscillate in both the  $x$  and  $y$  directions in an attempt to follow the curved electric field between two electrodes (field lines can be seen in fig. 1). Gravity provides a centripetal force for the curved oscillations. The particles oscillation height depends on the force of gravity, the time average force in  $y$ , and the inertial force from the particle following a curved path.

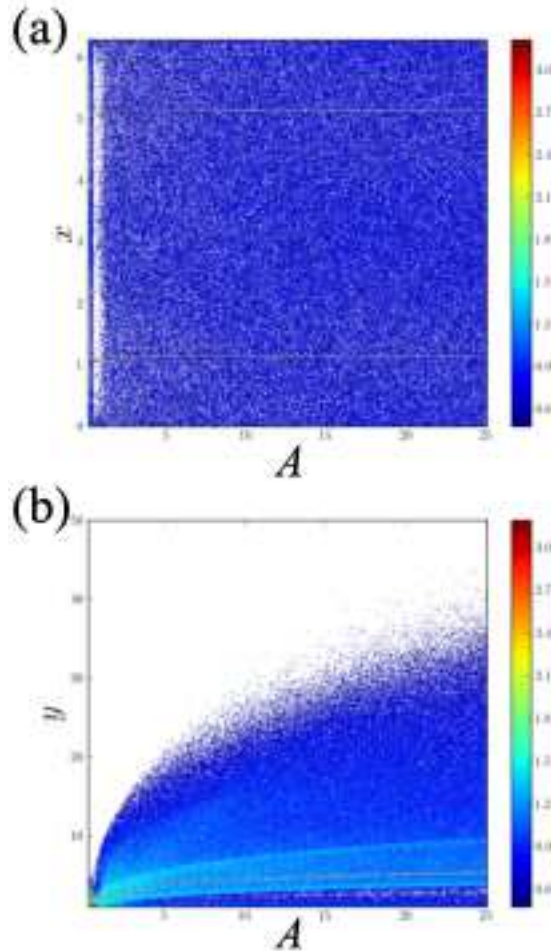


FIG. 11. Bifurcation diagram for  $\beta = 0.1$  made with same methods as 3 with projections of the final Poincaré section onto the (a)  $x$  axis and (b) the  $y$  axis.

In fig. 11b the background of scattered points are seen to be restricted to a domain of  $y$

which depends on  $A$ . The scattered points are transient motions that take a long time to completely die out for some initial conditions. For these parameters, as  $t \rightarrow \infty$  all initial conditions are in the basin of attraction for one of the two attractors.

For  $\beta = 0.05$  a strange attractor exists, shown for  $A = 9.0$  projected onto the  $x$  and  $y$  phase planes in fig. 12 respectively. If a stable limit cycle can not exist because  $\beta$  is too small or  $A$  is too large then the only type of motion found is the strange attractor in fig. 12 or a qualitatively similar strange attractor. The strange attractor is robust for variations in  $A$  as it only grows (shrinks) in the  $y$ ,  $\dot{y}$  directions when  $A$  is increased (decreased). The largest Lyapunov exponent for  $A = 9.0$  is  $0.134 \pm 0.003$ .

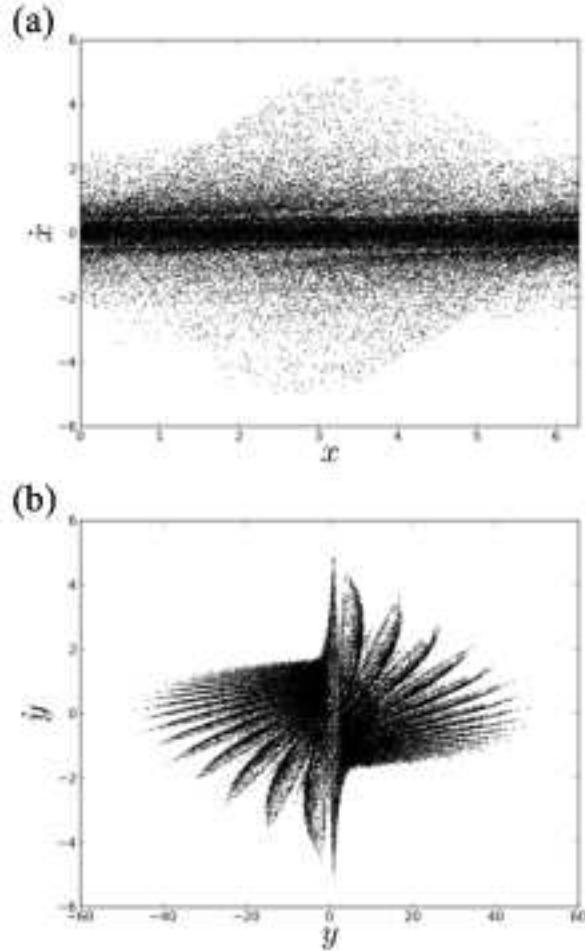


FIG. 12. Poincaré section of the chaotic attractor found in the 2D EC phase space for  $A = 9.0$  and  $\beta = 0.05$  plotted onto the (a)  $x, \dot{x}$  plane and (b)  $y, \dot{y}$  plane where we have mapped Poincaré sections after odd numbered reflections from the surface to below the surface in order to see the structure of the strange attractor more clearly. Made with same method as 6.

Even though independent variations of the damping are much more difficult to achieve experimentally we find that these variations produce slightly more interesting bifurcation diagrams. In fig. 13 we show  $x$  and  $y$  "bifurcation" diagrams for  $A = 9.0$ . In fig. 13a,b we show results for  $\beta < 2.0$  and in fig. 13c,d we show results for  $0.25 < \beta < 2.5$ . Figure 13a starts with a background of scattered points coexisting with two fixed points between the electrodes which is maintained for  $0.0 < \beta < 0.15$ . For  $\beta > 0.9$  the chaotic trajectory (fig. 12) drops out and only the stable fixed points exist until  $\beta \approx 0.9$ . For  $0.9 < \beta < 1.1$  the fixed points quickly loose their stability to a brief period of what misleadingly appears as another chaotic regime (explanation below). For  $\beta > 1.1$  two new stable fixed points are seen located in  $x$  at the position of the electrodes. In fig. 13b we only show the bifurcation diagram for  $0.2 < \beta < 2.0$  in order to show the most important features. In this diagram a red line, representing the two initial stable fixed points at the same value of  $y$ , becomes unstable at  $\beta \approx 0.9$ . We then see more scattered points which are more localized in  $y$  than in  $x$ . Then two new fixed points appear out of the unstable region for  $\beta > 1.1$ . The two fixed points in  $y$  after  $\beta \approx 1.1$  show that there are now four fixed points in the  $x, y$  plane. The two new fixed points located over each electrode represent a limit cycle that oscillates almost entirely in  $y$  with a small  $x$  component oscillation as well. These are stable limit cycles of particles attesting to follow the field lines near the electrodes. The most notable feature of fig. 13b, however, is the apparent reverse bifurcation cascade beginning at  $\beta = .29$  which we discuss in more detail at the end of this section.

The fixed points seen for  $\beta < 0.9$  in fig. 13 are the Poincaré sections of the same type of stable limit cycle discussed for fig. 11. The instabilities arise at  $\beta = 0.9$  because the particle can no longer maintain large oscillations that following the sharp curvature of the field directly between the electrodes. As the  $x$  component of their oscillations begins to damp out the time average force in  $x$ , which points towards the direction of constant potential (directly over the electrodes) begins to weaken the stability of the fixed points between the electrodes. The scattered points we see in fig. 13a for  $\beta = 1.0$  are the result of the competing stabilities of the fixed points between the electrodes and the fixed points above the electrodes. This competition creates a regime where particles will oscillate about any point in  $x$  but only about specific values of  $y$  in an attempt to follow the local field oscillation. These fixed points in the Poincaré sections may be described as being asymptotically stable in  $y$  and Lyapunov stable in  $x$ . Meaning that a particle oscillating at a some  $x$  will continue to oscillate about

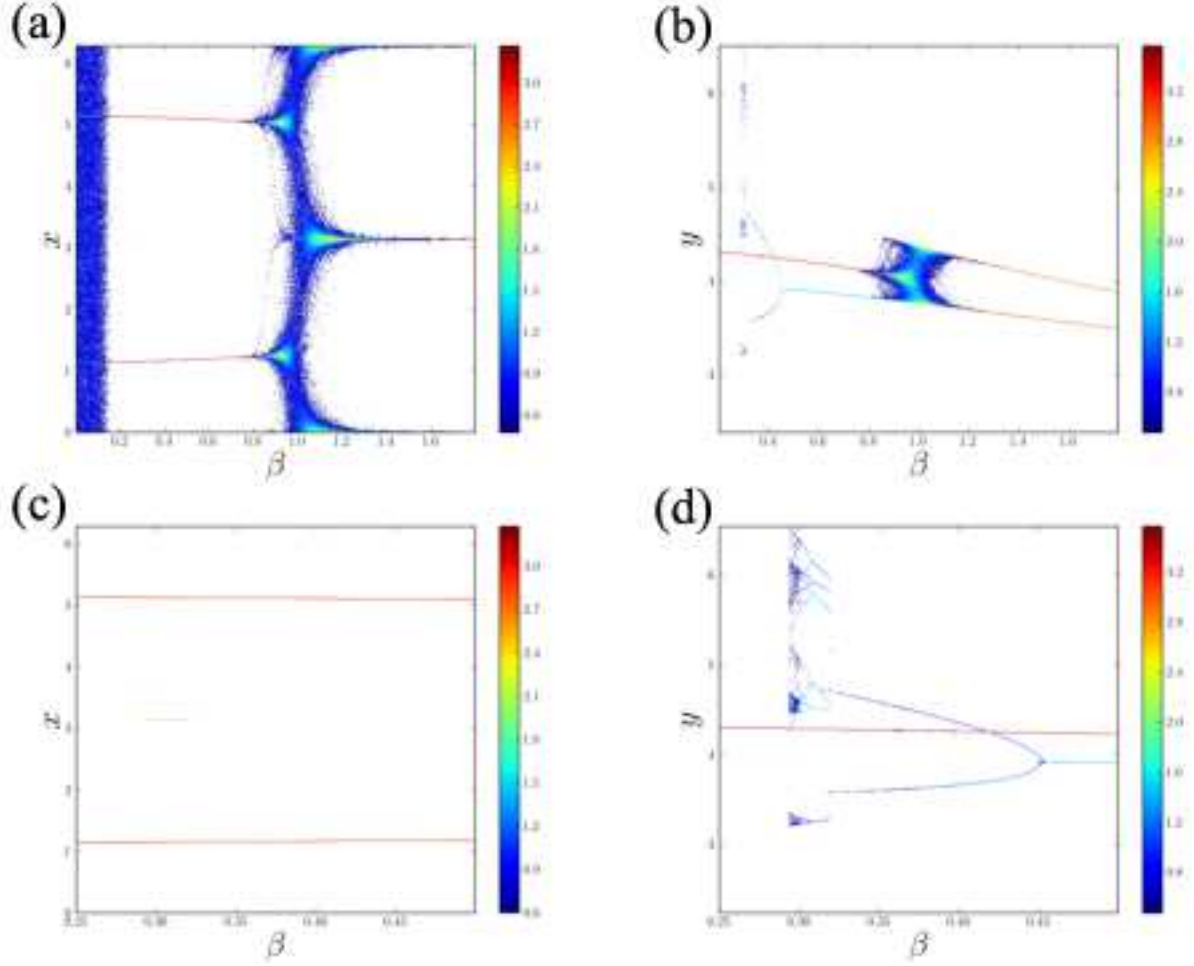


FIG. 13. Bifurcation diagram for variation in  $\beta$  with  $A = 9.0$ . Final Poincaré sections projected on to (a)  $x$  axis  $0.0 < \beta < 1.8$ , (b)  $y$  axis  $0.2 < \beta < 1.8$ . In (c) (projections onto  $x$  axis) and (d) (projections onto  $y$  axis) we show bifurcation diagrams for  $0.25 < \beta < 5$  to highlight the reverse bifurcation sequence.

that location unless there is a small perturbation in  $x$  after which it will oscillate about its new perturbed location. By Contrast small perturbations in  $y$  of an oscillations will push the particle out of equilibrium and it will experience a restoring force back to its original position. The resulting attractor appears as a line in the Poincaré sections. As we continue to increase  $\beta$  past 1.0 the time average force in  $x$  begins to dominate particle behavior. The fixed points that become most clear for  $\beta > 1.1$  represents stable oscillations in  $y$  above an electrode. The particles settle at a height above the surface for which the time averaged force in  $y$  and  $g$  are balanced.

Figure 13c shows the only actual bifurcation sequence found for the 2D EC, but from fig.



13d we see that this is actually behavior for particles constrained to  $1D$  motion in  $y$  directly above electrodes. For this range of  $\beta$  the time average force in  $x$  is not prevalent enough to prevent stable oscillations between the electrodes, as those are apparent in fig. 13c,d as well, but it is substantial enough to constrain the oscillations of particles near electrodes to motion directly above them. It is interesting to note the existence of such behavior in this model. We do not investigate it in any detail because observation of any such dynamical behavior in a stable reproducible way would be extremely difficult experimentally and has never been discussed in the literature.

## VI. CONCLUSION

We have studied the dynamics of a single particle in a 2-phase EC. We have separately considered the case of particle motion constrained to the surface of an EC for small interaction amplitude ( $1D$  EC) and the case of particle motion above the surface when the interaction amplitude is sufficiently large to lift the particle off of the surface ( $2D$  EC). We find a wide variety of possible stable limit cycles with different periodicities in the  $1D$  EC and show the bifurcations of fixed points in the Poincaré sections for variations in  $A$ . For limit cycles in the  $1D$  EC we calculate Floquet stability multipliers in order to analyze the transitions found in the bifurcation diagrams. We show that in the  $1D$  system it is possible to have different trajectories coexisting for the same values of  $A$  and  $\beta$ . In particular we find a chaotic trajectory that coexists with two asymptotically stable propagating trajectories having  $\pm\dot{x}$  velocities respectively. We also find that in the  $1D$  EC a transition of a limit cycle in or out of stability can happen discontinuously over small variations in  $A$ . In general the number of these discontinuous trajectories is greater for smaller values of  $\beta$ . We find a very different picture in the  $2D$  EC. Starting with the well known stable oscillations between two electrodes<sup>5,9,16,17,34</sup> we show how the height of this limit cycle depends on the interaction amplitude. In an interesting transition occurring for increasing values of  $\beta$ , the limit cycles loses its asymptotic stability in  $x$  and a line attractor in the Poincaré sections briefly describe particle behavior. Further increase of  $\beta$  leads to the asymptotic stability of  $1D$  limit cycles in  $y$  located directly above the electrodes. In both the  $2D$  and the  $1D$  models, we find chaotic motion of particles for particular parameter values. However, the transition from stable limit cycles to chaos is fundamentally different in the two models. In

the 1D EC a chaotic trajectory comes out of a period doubling cascade. In the 2D EC, the surface interferes with what would otherwise be a stable limit cycle and the result is chaotic motion.

By showing the general structure of particle dynamics for various values of the dimensionless parameters  $A$  and  $\beta$ , we develop a better understanding of how to induce and avoid certain types of particle behavior. We believe that the sensitivity of limit cycle periodicity on the interaction amplitude may be useful in particle sorting/separation applications. Particles with different charge-to-mass-ratios will fall into different regimes of the parameter space. Particles with charge-to-mass-ratios that place them in a regime of non-propagating stable motion (in either the 1D or 2D EC) will be trapped by the EC. For example, a particle in the 1D EC could be trapped in the  $\beta = 0.1$  and  $0.0 < A < 0.26$  regime. The EC may be configured so that particles of a slightly different charge-to-mass-ratio exhibit chaotic behavior by falling into the  $\beta = .1$ ,  $0.27 < A < 0.33$  regime resulting in slow mitigation over time.

The 2-phase EC is an attractive candidate for many particle manipulation and control applications, especially for dust and particle mitigation<sup>5</sup>. We have shown that there exists two dominate regimes of particle behavior in the 2D EC; one of which is stable oscillations, the other is chaotic. Therefore for EC mitigation applications it is necessary to understand the role of the surface as it is the primary instigator of non-stable particle trajectories. Mitigation efficiencies could be improved by an EC design in which most of the particles fall into chaotic motion. This can be done by tuning the EC parameters so that charge-to-mass-ratios of interest will exist in an area of the parameter space for which no stable motion is possible. For many real applications, we certainly would face a system of multiple particles. The analysis provided in the current paper is useful for a system of dilute particle density, for which the separation distance between particles is large enough that each particle's motion can be considered independent. While these results cannot be directly carried over to the case of more concentrated particle flows, they nevertheless provide an important step in understanding the dynamics of the 2-phase EC.

## ACKNOWLEDGMENTS

This work was supported by NASA Space Grant Consortium under grant numbers NNX10AK67H and NNX08AZ07A. We would also like to acknowledge Chris Danforth for his insights, suggestions, and guidance.

## Appendix A: Solving for the Electric Potential of a 2-Phase Electric Curtain

We can greatly simplify the problem of solving for the potential of an infinite series of parallel electrodes of infinite long length by rotating our coordinate system onto the complex plane and then making an appropriate conformal transformation. Here we use a similar procedure to that used by Masuda and Kamimura<sup>17</sup> to solve for the electric potential and field of the 2-phase EC. We start by defining the plane of the electrodes to be the  $x, z$  plane. The electrodes are infinitely long running parallel to the  $z$ -axis and are spaced evenly along the  $x$ -axis. We label . The  $y$ -axis is perpendicular to the plane of the electrodes. We define the wavelength to be twice the distance between adjacent electrodes and label them from 1, 2, ...,  $n$  respectively. The electric potential applied to the adjacent electrodes are 180 degrees out of phase so we express the charge per unit length on each electrode as

$$Q_n = Q \cos \omega t - (n - 1)\pi \quad (\text{A1})$$

where  $n$  denotes the electrode of interest; i.e.  $n = 1, 2, 3, \dots \infty$ . We choose to solve for the potential in the complex plane  $u, iv$ . The mapping is accomplished through the conformal transformation:

$$e^{(y+ix)2\pi/\lambda} = u + iv \quad (\text{A2})$$

introduced by Masuda and Kamimura<sup>17</sup>. This transformation maps an infinite set of electrodes onto a unit circle containing only two points. Electrodes 1, 3, 5... map to the same location in the  $u, v$  plane as electrode 1. It is also true that the electrodes 4, 6, 8... map to electrode 2 in the  $u, v$  plane and indeed all electrodes on  $x$  map to the two points on the  $u$ -axis. We can now solve for the electric potential in the  $u, v$  plane and transform our result back onto the  $x, y$  plane. Since the electrodes are infinitely long, we may express a two dimensional electric potential produced by the two neighboring electrodes as,

$$\Phi(u, v) = \sum_{n=1}^2 \frac{-Q_n}{2\pi\epsilon_0} \ln r_n, \quad (\text{A3})$$

where  $n$  denotes the  $n^{\text{th}}$  electrode,  $Q_n$  is given by Eq. (A1) and  $r_n$  is the distance between the point of interest  $(u, v)$  of the field coordinates and the source coordinates  $(u', v')$  of the  $n^{\text{th}}$  electrode:

$$r_n = \sqrt{(u - u'_n)^2 + (v - v'_n)^2} \quad (\text{A4})$$

Using Eq. (A4) we can express  $u$  and  $v$  in terms of  $x$  and  $y$  and find the corresponding electric potential in the  $x, y$  plane:  $u = \text{Re}[e^{k(y+ix)}]$ ,  $v = \text{Im}[e^{k(y+ix)}]$ . We find that  $r_n = \sqrt{2e^{ky}(\cosh ky - \cos k(x - x'_n))}$ . The potential can now be expressed in terms of only  $x$ , and  $y$  as

$$\Phi(x, y) = \sum_{n=1}^2 \frac{-Q}{4\pi\epsilon_0} \cos(\omega t - (n-1)\pi) \{\ln 2 + ky + \ln(\cosh ky - \cos k(x - x'_n))\}. \quad (\text{A5})$$

We can simplify this equation further by substituting in  $x'_n = \frac{(n-1)\lambda}{2}$  and noticing that  $\sum_{n=1}^2 \cos(\omega t - (n-1)\pi) = 0$  and only  $\ln(\cosh ky - \cos k(x - x'_n))$  in  $\{ \}$  survives, thus

$$\Phi(x, y) = \frac{-Q}{4\pi\epsilon_0} \cos \omega t \ln \frac{\cosh ky + \cos kx}{\cosh ky - \cos kx} \quad (\text{A6})$$

Since  $\vec{E} = -\nabla\Phi$ , we obtained Eq. (2) and Eq. (2).

## Appendix B: Floquet Stability Analysis

Here we explicitly show the methods for stability analysis of 1D EC limit cycles. In order to quantify the stability of a period- $p$  limit cycle we use Floquet theory<sup>27</sup>. For a period- $p$  fixed point  $\mathbf{r}_{fp}$  (for  $\mathbf{r}_{fp} = (x_{1fp}, x_{2fp})$ ) under  $\mathbf{T}^p$  (Poincaré map of period- $p$ ) the stability of  $\mathbf{r}_{fp}$  for  $\mathbf{T}^p$  expresses the stability of the limit cycle period- $p$   $\{\mathbf{r}_{fp}\}$ . For the rest of this discussion we work with the non-autonomous expressions of the equations of motion and therefore we will refer to  $\{\mathbf{r}_{fp}\}$  as  $\mathbf{r}_{fp}(t)$  from here on. We now introduce the linearized-map matrix  $\mathbf{DT}^p$ , which acts on the period- $p$  fixed point  $\mathbf{r}_{fp}$  in the expected way i.e.  $\mathbf{DT}^p \mathbf{r}_{fp} = \mathbf{r}_{fp}$ . The stability of  $\mathbf{r}_{fp}$  is then found by finding the eigenvalues of  $\mathbf{DT}^p$  where  $\mathbf{DT}^p$  is found by

integrating the linearized differential equations of motion for a trajectory close to  $\mathbf{r}_{fp}(t)$ . We find a close perturbation of  $\mathbf{r}_{fp}(t)$ , which we call  $\alpha(t) \equiv (x_{1\alpha}, x_{2\alpha})$ , by using an infinitesimal perturbation to  $\mathbf{r}_{fp}$  as the initial conditions to solve for the motion  $\alpha(t)$ . The time dependent equations of motion for  $\alpha(t)$  may be expressed as

$$\begin{pmatrix} \dot{x}_{1\alpha} \\ \dot{x}_{2\alpha} \end{pmatrix} = \mathbf{J}(t) \begin{pmatrix} x_{1\alpha} \\ x_{2\alpha} \end{pmatrix}, \quad (\text{B1})$$

where  $\mathbf{J}(t)$  is the Jacobean matrix for  $\mathbf{r}_{fp}(t)$  and is found to be:

$$\mathbf{J}(t) = \begin{pmatrix} 0 & 1 \\ \frac{\cos t \cos x_{1fp} \cosh 1 (\cosh 2 + \cos 2x_{1fp} - 2)}{(\cos^2 x_{1fp} - \cosh^2 1)^2} & -\beta \end{pmatrix}. \quad (\text{B2})$$

In general the solution to  $\alpha(t)$  may be expressed as

$$\begin{pmatrix} x_{1\alpha}(t) \\ x_{2\alpha}(t) \end{pmatrix} = x_{1\alpha}(0) \mathbf{w}^1(t) + x_{2\alpha}(0) \mathbf{w}^2(t), \quad (\text{B3})$$

where  $\mathbf{w}^1(t)$  and  $\mathbf{w}^2(t)$  are the two linearly independent solutions which can be written together as

$$\mathbf{W}(t) = \begin{pmatrix} w_1^1(t) & w_2^1(t) \\ w_1^2(t) & w_2^2(t) \end{pmatrix}. \quad (\text{B4})$$

This is called the solution matrix. We can now express Eq. (B3) as

$$\begin{pmatrix} x_{1\alpha}(t) \\ x_{2\alpha}(t) \end{pmatrix} = \mathbf{W}(t) \begin{pmatrix} x_{1\alpha}(0) \\ x_{2\alpha}(0) \end{pmatrix}, \quad (\text{B5})$$

where  $\mathbf{W}(0)$  is necessarily the identity matrix. Now we see that  $\mathbf{W}(t)$  is the linearized flow  $\mathbf{DT}^t$  and by substituting Eq. (B5) into Eq. (B1) we obtain the initial value problem

$$\dot{\mathbf{W}}(t) = \mathbf{J}(t) \mathbf{W}(t), \quad (\text{B6})$$

which we can solve for  $\mathbf{W}(t)$ . For the desired period- $p$ , namely the one associated with  $\mathbf{r}_{fp}(t)$ , we numerically integrate Eq. (B6) from  $t = 0$  to  $2\pi p$ , giving us the linearized map matrix  $\mathbf{DT}^p$ . The eigenvalues of this matrix are the Floquet stability multipliers of  $\mathbf{r}_{fp}(t)$  under the appropriate Poincaré map.

## REFERENCES

- <sup>1</sup>S. Masuda, “Booth for electrostatic powder painting with contact type electric field curtain,” (1974).
- <sup>2</sup>S. Masuda, M. Washizu, and I. Kawabata, “Movement of blood cells in liquid by nonuniform traveling field,” *IEEE Transactions on Industry Applications* **24**, 217–222 (1988).
- <sup>3</sup>L. C. Weiss and D. P. Thibodeaux, “Separation of seed by-products by and ac electric field,” *JAOCS* **61**, 886–890 (1984).
- <sup>4</sup>F. W. Schmidlin, “Development apparatus,” (1987).
- <sup>5</sup>M. Mazumder, R. Sharma, A. Biris, J. Zhang, C. Calle, and M. Zahn, “Self-cleaning transparent dust shields for protecting solar panels and other devices,” *Particulate Science and Technology* **25**, 5–20 (2007).
- <sup>6</sup>H. Kawamoto, “Some techniques on electrostatic separation of particle size utilizing electrostatic traveling-wave field,” *Journal of Electrostatics* **66**, 220–228 (2008).
- <sup>7</sup>H. Kawamoto, K. Seki, and N. Kuromiya, “Mechanism of travelling-wave transport of particles,” *Journal of Physics D: Applied Physics* **39**, 1249–1256 (2006).
- <sup>8</sup>G. Liu and J. Marshall, “Effect of particle adhesion and interactions on motion by traveling waves on an electric curtain,” *Journal of Electrostatics* **68**, 179–189 (2010).
- <sup>9</sup>G. Liu and J. Marshall, “Particle transport by standing waves on an electric curtain,” *Journal of Electrostatics* **68**, 289–298 (2010).
- <sup>10</sup>Z. Dudzicz, “Recording of dust particle oscillation path inside electric curtain by laser diode apparatus,” *Optica Applicata* **35**, 907–912 (2005).
- <sup>11</sup>F. W. Schmidlin, “Modes of traveling wave particle transport and their applications,” *Journal of Electrostatics* **34**, 225–244 (1995).
- <sup>12</sup>F. W. Schmidlin, “A new non-levitated mode of traveling wave toner transport,” *IEEE Transactions on Industry Applications* **27**, 480–487 (1991).
- <sup>13</sup>J. M. Hemstreet, “Velocity distribution on the masuda panel,” *Journal of Electrostatics* **17**, 245–254 (1985).
- <sup>14</sup>J. M. Hemstreet, “Three-phase velocity distribution of lycopodium particles on the masuda panel,” *Journal of Electrostatics* **27**, 237–247 (1991).
- <sup>15</sup>J. Chesnutt and J. Marshall, “Simulation of particle separation on an inclined electric curtain,” *IEEE Transactions on Industry Applications* **49**, 1104–1112 (2013).

- <sup>16</sup>P. Atten, H. Pang, and J. Reboud, “Study of dust removal by standing wave electric curtain for application to solar cells on mars,” *IEEE Transactions on Industry Applications* **45**, 75–86 (2009).
- <sup>17</sup>R. Sims, A. Biris, J. Wilson, C. Yurteri, M. Mazumder, C. Calle, and C. Buhler, “Development of a transparent self-cleaning dust shield for solar panels,” *Proceedings ESA-IEEE Joint Meeting on Electrostatics*, 814 (2003).
- <sup>18</sup>S. Masuda and T. Kamimura, “Approximate methods for calculating a non-uniform travelling field,” *Journal of Electrostatics* **1**, 351–370 (1975).
- <sup>19</sup>S. Kim and B. Hu, “Bifurcations and transitions to chaos in an inverted pendulum,” *Physical Review E* **58**, 3028–3035 (1998).
- <sup>20</sup>E. Butikov, “An improved criterion for kapitza’s pendulum stability,” *Journal of Physics A: Mathematical and Theoretical* **44**, 295292 (2011).
- <sup>21</sup>J. Starrett and R. Tagg, “Control of a chaotic parametrically driven pendulum,” *Physical Review Letters* **74**, 1974–1977 (1995).
- <sup>22</sup>A. Johnson and J. Rabchuk, “A bead on a hoop rotating about a horizontal axis: A one-dimensional ponder motive trap,” *American Journal of Physics* **77**, 1039–1048 (2009).
- <sup>23</sup>L. Ruby, “Applications of the mathieu equation,” *American Journal of Physics* **64**, 39–44 (1996).
- <sup>24</sup>M. Abramowitz and I. A. Stegun, *Handbook of Mathematical Functions*, 2nd ed. (Dover Publications, New York, 1965).
- <sup>25</sup>N. W. McLachlan, *Theory and Application of Mathieu Functions*, 1st ed. (Oxford University Press, London, 1947).
- <sup>26</sup>N. Brilliantov and T. Poschell, “Rolling as a continuing collision,” *The European Physical Journal B* **12**, 299–301 (1999).
- <sup>27</sup>J. Guckenheimer, *Nonlinear Oscillations, Dynamical Systems, and Bifurcations of Vector Fields* (Springer-Verlag, New York, 1983).
- <sup>28</sup>P. Morse and K. Feshbach, *Methods of Theoretical Physics* (McGraw-Hill Book Company, New York, 1953).
- <sup>29</sup>H. Gunderson, H. Rigas, and F. S. VanVleck, “A technique for determining stability regions for the damped mathieu equation,” *SIAM Journal of Applied Mathematics* **26**, 345–349 (1974).
- <sup>30</sup>S. Lefschetz, *Differential Equations Geometric Theory*, 2nd ed. (Dover Publications, New

York, 1977).

- <sup>31</sup>J. Wu and W. L. Nyborg, “Ultrasound, cavitation bubbles and their interaction with cells, invited review paper,” *Advanced Drug Delivery Reviews* **60**, 1103–1116 (2008).
- <sup>32</sup>J. Thompson and H. Stewart, *Nonlinear Dynamics and Chaos*, 2nd ed. (Wiley, New York, 2002).
- <sup>33</sup>K. T. Alligood, T. D. Sauer, and J. A. Yorke, *Chaos - an introduction to dynamical systems* (Springer, New York, 1996).
- <sup>34</sup>Z. Dudzicz, “Electrodynamics of charged dust particles and repulsion force within plane-type electric curtain,” *Journal of Electrostatics* **51-52**, 111–116 (2001).
- <sup>35</sup>S. Masuda, K. Fujibayashi, K. Ishida, and H. Inaba, “Confinement and transportation of charged aerosol clouds via electric curtain,” *Electrical Engineering in Japan* **92**, 43 (1972).
- <sup>36</sup>C. I. Calle, M. K. Mazumder, C. D. Immer, C. R. Buhler, J. S. Clements, P. Lundeen, A. Chen, and J. Mantovani, “Controlled particle removal from surfaces by electrodynamic methods for terrestrial, lunar and martian environmental conditions,” *Journal of Physics: Conference Series* **142**, 012073 (2008).